MID-AMERICA TRANSPORTATION CENTER

Report # MATC-UNL: 004-51

Final Report

WBS: 27-1121-0005-004-51

Lidar-Based Vibration Monitoring for Assessing Safety of Damaged Bridges

Christine E. Wittich, PhD
Assistant Professor
Department of Civil and Environmental Engineering
The University of Nebraska-Lincoln

Richard L. Wood, PhD
Associate Professor

Khalid H. Alkady, MS
PhD Candidate

2024

A Cooperative Research Project sponsored by
U.S. Department of Transportation- Office of the Assistant Secretary for Research and Technology

Lidar-Based Vibration Monitoring for Assessing Safety of Damaged Bridges

Christine E. Wittich, Ph.D.
Assistant Professor
Department of Civil and Environmental Engineering
University of Nebraska-Lincoln

Khalid H. Alkady, M.S.
Ph.D. Candidate
Department of Civil and Environmental Engineering
University of Nebraska-Lincoln

Richard L. Wood, Ph.D.
Associate Professor
Department of Civil and Environmental Engineering
University of Nebraska-Lincoln

A Report on Research Sponsored by

Mid-America Transportation Center

University of Nebraska–Lincoln

December 2022

Technical Report Documentation Page

1. Report No. 25-1121-0005-004-51	2. Government Accession No.	3. Recipient's Catalog No.
4. Title and Subtitle Lidar-Based Vibration Monitoring for Assessing Safety of Damaged Bridges		5. Report Date September 2024
		6. Performing Organization Code
7. Author(s) Christine E. Wittich, 0000-0002-2678-7310 Richard L. Wood, 0000-0002-8642-2217 Khalid H. Alkady, 0000-0001-6820-0736		8. Performing Organization Report No. 25-1121-0005-004-51
9. Performing Organization Name and Address Mid-America Transportation Center Prem S. Paul Research Center at Whittier School 2200 Vine St. Lincoln, NE 68583-0851		10. Work Unit No. (TRAIS)
		11. Contract or Grant No.
12. Sponsoring Agency Name and Address Office of the Assistant Secretary for Research and Technology 1200 New Jersey Ave., SE Washington, D.C. 20590		13. Type of Report and Period Covered March 2020 – December 2022
		14. Sponsoring Agency Code MATC TRB RiP No. 91994-59
15. Supplementary Notes		

16. Abstract

While there has been substantial research conducted on the use of Ground-Based Lidar (GBL) in monitoring the static deformation of civil structures, there have been only a few studies on the use of GBL in monitoring the dynamic vibrations of structures, which is critical information for structural health monitoring (SHM). Robust GBL-based vibration monitoring frameworks can address some of the limitations of traditional contact-based SHM frameworks, which include limited number of sensors and the need for physical access to place instrumentation. The main objective of this study is to develop and comprehensively validate a novel end-to-end framework to monitor the dynamic vibrations of structures using GBL through extensive experimentation in a controlled laboratory environment. In this project, a novel two-step spatio-temporal algorithm was developed to extract the dynamic vibrations of structures from the dynamic point clouds. The framework leverages the Density-based Spatial Clustering of Applications with Noise (DBSCAN) and change detection algorithms. The impact of several GBL-based parameters on the accuracy of the operational modal analysis results was investigated across six single-degree-of-freedom structures with unique natural frequencies. The GBL-based parameters included the resolution, quality, and point-to-point distance of the dynamic point clouds. Accelerometers and infrared-based sensors were used for the validation of GBL measurements and operational modal analysis results. This study concludes that GBL can be used reliably for remotely monitoring the dynamic response of structures at a high spatial resolution. However, further research is warranted to evaluate the full extents of the proposed framework.

17. Key Words Ground-Based Lidar; System Identification; Remote Sensing;	18. Distribution Statement

19. Security Classif. (of this report) Unclassified	20. Security Classif. (of this page) Unclassified	21. No. of Pages 47	22. Price

Table of Contents

List of Figures

List of Tables

Disclaimer

The contents of this report reflect the views of the authors, who are responsible for the facts and the accuracy of the information presented herein. This document is disseminated in the interest of information exchange. The report is funded, partially or entirely, by a grant from the U.S. Department of Transportation's University Transportation Centers Program. However, the U.S. Government assumes no liability for the contents or use thereof.

Abstract

While there has been substantial research conducted on the use of Ground-Based Lidar (GBL; i.e., Terrestrial Laser Scanners) in monitoring the static deformation of civil structures, there have been only a few studies on the use of GBL in monitoring the dynamic vibrations of structures, which is critical information for structural health monitoring (SHM). Robust GBL-based vibration monitoring frameworks can address some of the limitations of traditional contact-based SHM frameworks, which include a limited number of sensors and the need for physical access to place instrumentation. The main objective of this study is to develop and comprehensively validate a novel end-to-end framework to monitor the dynamic vibrations of structures using GBL through extensive experimentation in a controlled laboratory environment. In this project, a novel two-step spatio-temporal algorithm was developed to extract the dynamic vibrations of structures from the dynamic point clouds. The framework leverages the Density-based Spatial Clustering of Applications with Noise (DBSCAN) and change detection algorithms. The impact of several GBL-based parameters on the accuracy of the operational modal analysis results was investigated across six single-degree-of-freedom structures with unique natural frequencies. The GBL-based parameters included the resolution, quality, and point-to-point distance of the dynamic point clouds. Accelerometers and infrared-based sensors were used for the validation of GBL measurements and operational modal analysis results. This study concludes that GBL can be used reliably for remotely monitoring the dynamic response of structures at a high spatial resolution. However, further research is warranted to evaluate the full extents of the proposed framework.

Chapter 1 Introduction

1.1 Background

The accelerated aging and deterioration of civil infrastructure systems are among the most pressing challenges to the US economy in the 21st century. According to the American Society of Civil Engineers' 2021 Infrastructure Report Card [1], America's civil infrastructure has a grade point average (GPA) of C- on an A through F grade scale. A funding gap of ~$2.6 trillion is needed over the next 10 years for the US civil infrastructure to achieve a GPA of B (i.e., good repair condition). To reduce this massive bill of repair and maintenance in the long run, there is a critical need to develop robust structural health monitoring (SHM) solutions that are capable of accurately detecting and quantifying structural deterioration at an early stage. The early diagnosis and repair of structural damage (i.e., preventative maintenance) can significantly reduce the long maintenance backlogs and prolong the service life of our nation's infrastructure. Furthermore, due to the lack of funding available to repair all structures in need, SHM solutions can be used to quantitatively prioritize structures for repair and maintenance based on their operational condition and health.

Analysts commonly rely on vibration-based structural health monitoring (SHM) methods to evaluate the operational conditions of structures in service [2-9]. However, robust and accurate vibration data is critical for vibration-based structural health monitoring (SHM) applications, including damage diagnostics, prognostics, and model updating and calibration [2-4]. Remote sensing technology (i.e., laser scanners and cameras) can be employed to conduct full-field dynamic monitoring of structures [14-37] and address some of the limitations of traditional contact-based techniques of SHM, including limitations on the number of sensors and the need for physical access to place instrumentation [3, 10-13].

Although vision-based frameworks (i.e., using stationary cameras or uncrewed aerial systems (UAS)) have shown promise in conducting full-field monitoring of structures, these frameworks are generally computationally expensive, sensitive to environmental conditions (i.e., illumination, fog, surface preparation), and oftentimes need high-contrast targets to be placed on the structure-of-interest [14-32].

Ground-Based Lidar (i.e., GBL; also known as Terrestrial Laser Scanning) is a remote sensing platform that typically acquires dense 360-degree point clouds representing the position of objects within the unit's line of sight in a Cartesian coordinate system. GBL has been widely used in monitoring the long-term deformation of large civil structures due to: 1) the high spatial resolution of the point clouds generated, 2) the robustness of the Lidar technology to environmental conditions such as illumination, fog and surface preparation, and 3) unlike camera systems, GBL has a long range of detection (i.e., up to 100's of meters) [36-41]. However, GBL can be modified to acquire successive narrow point clouds at high frequency, which enables remote full-field dynamic monitoring of structures at a very high spatial resolution, as shown in Figure 1.1.

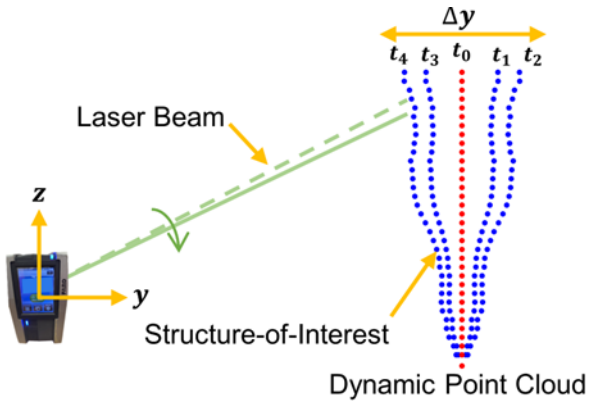

Figure 1.1 Schematic of Lidar-based dynamic monitoring of structures

1.2 Problem Statement

While there has been substantial research conducted on the use of GBL in monitoring the static deformation of civil structures, there have been only a few studies on the use of GBL in monitoring the dynamic vibrations of structures [36-41]. Previous studies highlight promising results for quantifying structural vibrations from GBL, however, several research gaps remain. First, GBL-based dynamic monitoring has not been validated beyond a few case study structures. To more adequately reflect the range of civil infrastructure, the GBL-based dynamic monitoring technology needs to be evaluated across a broad range of dynamic properties that represent typical civil infrastructure systems while using traditional and reliable sensing modalities for validation. Second, the impact of lidar-based variables (i.e., quality, resolution and point-to-point distance of dynamic point clouds) on the accuracy of the results has not been thoroughly investigated. Third, methods for processing dynamic point clouds are few and they do not scale well to different use cases. This project aims to address these gaps through the development and validation of end-to-end frameworks to monitor the dynamic response of structures using GBL.

1.3 Scope and Objectives

The objectives of this study are: 1) develop a novel spatio-temporal framework to autonomously extract the dynamic vibrations of the structure of interest from the dynamic point clouds; 2) extensively investigate the robustness of GBL-based dynamic monitoring across a range of structures with various dynamic characteristics under different lidar variables; and 3) validate GBL OMA results using infrared-based sensors and accelerometers.

1.4 Report Organization

The report is organized as follows:

- **Chapter 2:** discusses the prior efforts conducted in developing algorithms to detect change in point cloud and the use of GBL to monitor the dynamic response of structures
- **Chapter 3:** proposes an end-to-end framework for monitoring the dynamic response of structures using FARO x130. The chapter includes the specifications of the lidar dynamic setup used in this report. End-to-end spatial clustering and voxelization as well as change detection algorithms for the processing of dynamic point clouds are discussed in detail.
- **Chapter 4:** discusses the extensive experimental program used for the validation of the proposed framework. The experimental results were compared to those of accelerometers and an optical motion tracking system to evaluate the robustness of the proposed GBL-based dynamic monitoring framework.
- **Chapter 5:** discusses the key findings of the report and proposes future work.

Chapter 2 Literature Review

The literature review section discusses prior research efforts conducted in the areas of 1) development of change detection algorithms, and 2) the use of Ground-based Lidar to monitor the dynamic response of structures.

2.1 Change Detection Techniques

Change Detection (CD) is the process of identifying differences between multi-temporal remotely sensed datasets (i.e., images/videos and point clouds) of an object. CD techniques are very critical for meaningful and accurate interpretations of the differences between multi-temporal remotely sensed datasets [44]. Change detection techniques are widely used in several applications (i.e., structural monitoring, geomorphology, urban and forest inventory). Terrestrial Laser Scanners (TLS), Mobile Laser Scanners (MLS), and ALS. Generally, there are two main approaches for CD: 1) direct comparison and 2) post-classification comparison (PCC). The direct comparison relies on the comparison between raw datasets collected at different time epochs after registration without classification or object/feature detection. On the other hand, PCC relies on a comparison between already classified datasets [44, 45], which requires additional processing steps before applying change detection techniques. Change detection techniques can be based on 1) algebra, 2) transformation, 3) classification, 4) advanced models, 5) GIS, 6) visual analysis, or 7) other change detection techniques [46]. In addition, Mishra et al. [47] and Coppin et al. [48] reviewed and summarized the change detection techniques and frameworks used in detecting changes on the surface of the earth and ecosystem, respectively.

For direct-comparison-based CD approaches, point-to-point, point-to-surface, surface-to-surface, or subset-to-subset (i.e., Hausdorff distance) distance is computed to quantify the amount of change occurred between point clouds. Girardeau-Montaut et al. [49] developed a framework

for direct comparison between two 3D lidar point clouds of the same scene, which were collected at different time epochs. The framework was based on partitioning the point clouds into octree structures to significantly reduce the computation cost and time. Three different strategies of CD calculations were evaluated: 1) the average distance between points, 2) best-fit plane orientation and 3) Hausdorff distance. The results showed that the Hausdorff distance outperformed the other two methods, and the octree-based framework significantly reduced the computation time. Lague et al. [50] developed a robust CD technique "Multiscale Model to Model Cloud Comparison" (M3C2) for direct comparisons between point clouds in an effort to address the limitations other CD techniques encounter, such as surface roughness-related errors. M3C2 does not include point-cloud meshing to avoid the loss of roughness and detailed topographical information and enhance the distance measurement process. Instead, in M3C2, the local distances between core points, which were subsets of points of the reference point cloud within a specific point-to-point spacing, the normal direction were computed with the incorporation of local roughness information. M3C2 was tested against various closest-point algorithms, and the results showed that M3C2 was very sensitive to small surface changes and independent of point intensity and roughness. For PCC, the datasets need to be classified first using unsupervised or supervised techniques, then CD is computed between recognized objects or features or clusters instead of points, and this is commonly used in applications involving datasets collected using Aerial Laser Scanner (ALS) [45].

Du et al. [51] developed an automatic change detection framework using old aerial image and new LiDAR data for detecting building changes in urban areas. Firstly, using aerial triangulation, the aerial images were registered and used to produce a dense point cloud. Then, the generated dense point cloud was co-registered with the LiDAR 3D point cloud using the Iterative

Closest Point (ICP) algorithm and resampled to a raster Digital Surface Model (DSM). The height difference and grey-scale similarity were computed as change indicators and the graph-cuts method was used for detecting the changes. Also, Pirasteh et al. [52] developed an algorithm for change detection and extraction of the building borders from point clouds collected by ALS. At first, the outliers were removed from the point clouds at different epochs, and then, the point clouds were co-registered and filtered. Then, the pre-processed and co-registered point clouds were converted into nDSM, where thresholding was applied to isolate buildings from the surroundings based on the altitude. After thresholding, detecting the changes that happened to buildings at two epochs became possible. The incorporation of Firefly and Ant Colony algorithms aided in the extraction of building borders. Furthermore, the efficiency of the proposed algorithm in extraction building boundaries was compared with the Mask Region-Based Convolutional Neural Network (R-CNN) algorithm using drone images. The results showed that the use of LiDAR data and the proposed algorithm gave better results than using the Mask R-CNN and drone images for the extraction of building boundaries.

Aijazi et al. [53] developed and evaluated a super-voxel-based approach for a segmentation-based classification of 3D urban point clouds collected by LiDAR. The approach began with voxelization, where the 3D points in the point cloud were grouped in cubical voxels based on the distance between the points and their neighbors. Then, the voxels were transformed into super-voxels, by assigning properties (i.e., mean R, G, and B values, surface normal, mean laser reflectance intensity value, geometrical center of a voxel, etc.) to them based on their constituting points. Afterward, the super-voxels of similar attributes were grouped together to form segmented objects using the link-chain method. The segmented objects were classified based on the comparison between the geometrical models and local descriptors of the segmented objects,

and pre-defined thresholds. Two metrics were developed to assess the segmentation and classification performances, and the results showed that the proposed approach achieved an overall accuracy in the vicinity of 90%.

Furthermore, Mukupa et al. [54] reviewed the use of TLS in change detection and deformation monitoring of several civil structures (i.e., tunnels, buildings, dams, etc.), and evaluated the point-cloud registration techniques used in quantifying the deformation of those structures. The discussed CD techniques included point-to-point, point-to-surface, and surface-to-surface-based deformation analyses. Several outstanding challenges of using TLS in the deformation monitoring of structures were identified, and a three-stage framework was developed to tackle those challenges. The three-stage framework consisted of the Multiscale Model to Model Cloud Comparison (M3C2) for change detection, piecewise alignment method, and block-to-point estimation for deformation analyses.

2.2 GBL Applications in Dynamic Monitoring

Despite the great success of lidar in monitoring static deformations, there have been only a handful of case studies that explored the use of GBL in monitoring the vibrations of civil structures. Gueguen et al. [33] monitored the dynamic response of a building using a coherent lidar. In this application, the lidar unit monitored the response of the building at a single location only and velocimeters were used for validation. Although the lidar measurements were significantly noisier than those of velocimeters, the operational modal analysis (OMA) results of lidar data were in good agreement with those of velocimeters. Moving beyond monitoring at a single point, Jatmiko and Psimoulis [34] monitored the dynamic response of a high-rise steel sculpture using a GBL operating at a fixed horizontal angle (i.e., vertical line-based scanning). The dynamic response along the height of the sculpture was captured at a sampling frequency of 24

Hz, and the natural frequency of the sculpture was estimated via modal analysis of the lidar data. More recently, Lee and Kim [35] monitored the response of two laboratory-scale structures using a low-cost multi-channel lidar. The authors developed several post-processing algorithms to correct the axes and tilt errors as well as data synchronization issues associated with this type of lidar unit. The lidar-based natural frequencies of the two structures were within 5% of those estimated from traditional sensing systems.

Furthermore, alternative vision-based systems can incorporate depth information and generate remotely sensed 3D dynamic point clouds, such as RGB-D sensors (i.e., Time-of-Flight (ToF) imagers), which have been successfully used to generate dynamic 3D point clouds of laboratory structures for system identification in a recent 2022 study [42]. Furthermore, Chesebrough et al. [43] estimated the natural frequencies and mode shapes of a cantilever beam using dynamic 3D point clouds generated using a plenoptic camera (i.e., a camera system that captures the direction of the light entered the camera to make depth measurements).

2.3 Summary and Knowledge Gaps

Previous studies highlight promising results for quantifying structural vibrations from GBL, however, several research gaps remain. First, GBL-based dynamic monitoring has not been validated beyond a few case study structures. To more adequately reflect the range of civil infrastructure, the GBL technique needs to be evaluated across a broad range of dynamic properties that represent typical civil infrastructure systems while using traditional and reliable sensing modalities for validation. Second, the impact of lidar-based variables (i.e., quality, resolution, point-to-point distance) on the accuracy of the results has not been thoroughly investigated. Third, methods for processing dynamic point clouds are few and they do not scale well to different use cases.

Chapter 3 Lidar Framework for Dynamic Response Extraction

This chapter presents the dynamic lidar setup used in this study and describes the proposed end-to-end frameworks to process the dynamic point clouds autonomously for civil system identification applications.

3.1 Equipment and Data Acquisition

In this study, a phase-based FARO Focus3D x130 laser scanner mounted on a helical adapter was used to acquire the dynamic response of structures remotely, as shown in Figure 3.1. The helical adapter allows the scanner's mirror to rotate vertically only at a fixed horizontal angle, which is known as the helical scan mode. The vertical mirror's field-of-view is from -150° to $+150^{\circ}$ with a scanner range of 130 m. Helical scans facilitate continuous line-based scanning without time delay (i.e., dynamic monitoring), where the scanner's sampling frequency corresponds to the total number of revolutions of the vertical mirror per second. Therefore, remote full-field monitoring of structures can be conducted through helical scans, where each point in the resulting dynamic point cloud is likened to a traditional sensor placed on the structure-of-interest. The resulting helical scan file consists of a series of sequentially time-stamped 2D point clouds (i.e., scanlines) of its field of view, which corresponds to the total number of complete revolutions done by the scanner's vertical mirror. The time-stamped scanlines are extracted from the original helical scan file using the open-source FARO Open software to generate a dynamic point cloud. The scanline files store the time stamp (i.e., automation time) of each data point acquired with a time resolution of 1μs as well as the position of each data point in the cartesian coordinate system format where Y is the horizontal distance from the scanner and Z is the height.

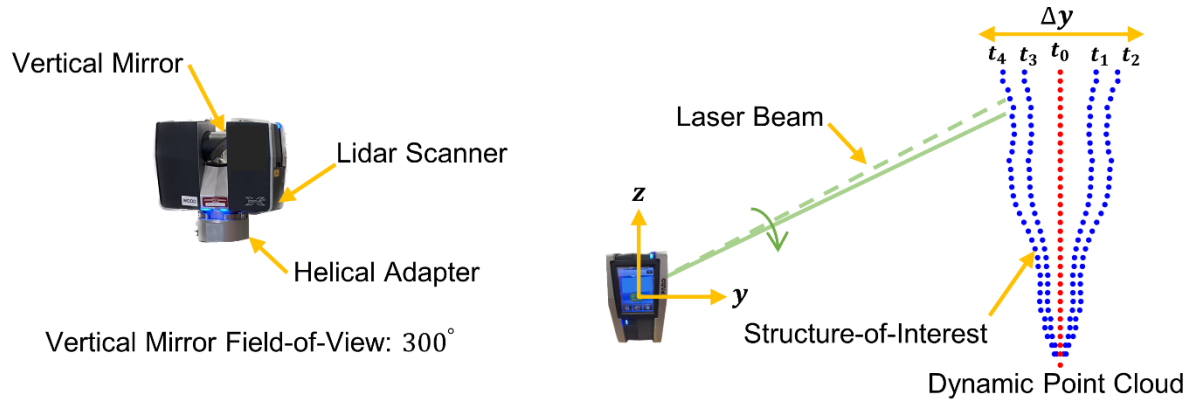

Figure 3.1 Lidar scanner and helical adapter

3.2 Dynamic Point Cloud Processing

A novel two-step spatio-temporal algorithm was developed to identify and extract the structural vibration information from the background scene within the helical scan files (i.e., dynamic point clouds). An overview of this algorithm is shown in Figure 3.2. The algorithm starts with spatial clustering and voxelization, where voxelization is the process of partitioning the point cloud into a regular three-dimensional grid to facilitate point tracking and monitoring. Each partition of this three-dimensional grid is referred to as a voxel. Then, a change detection algorithm extracts the dynamic response of each voxel which is a displacement time history at a given point on the structure. A dynamic point cloud is an array of sequentially time-stamped 2D point clouds, where clustering and voxelization of each 2D point cloud independently is computationally very demanding. To cluster and voxelize the entire dynamic point cloud efficiently, the proposed algorithm relies on clustering and voxelizing a reference point cloud (i.e., 2D point cloud at time $t = 0$) rather than processing every 2D point cloud in the dynamic point cloud independently. The spatial clustering and voxelization algorithm is presented in Figure 3.3. It can be assumed that real-world civil structures typically do not undergo large rigid-body displacements. Hence, it is expected that structural vibrations (i.e., small dynamic displacements relative to the structure's

geometry) will not lead to significant changes with respect to the distance between the structure-of-interest and GBL during dynamic monitoring. Therefore, the algorithm assumes that the row indices of the datapoints of the structure-of-interest are nearly identical across all the 2D point clouds generated over the duration of the test, which justifies clustering and voxelizing the entire dynamic point cloud based on the initial reference point cloud. For simplicity, each row in a 2D point cloud can be envisioned as a single lidar channel that measures the distance to a point in space.

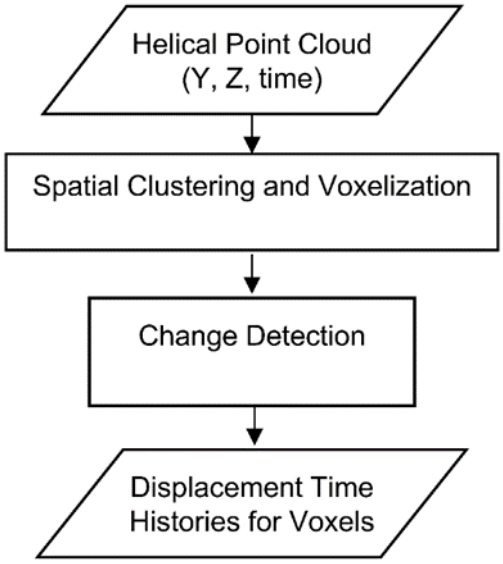

Figure 3.2 Overview of the end-to-end framework for processing dynamic point clouds

Figure 3.3 details the algorithm that clusters and voxelizes the reference point cloud, where the Density-based Spatial Clustering of Applications with Noise (DBSCAN) algorithm is utilized to partition the point cloud into clusters based on spatial density. The DBSCAN algorithm was chosen as it is suitable and robust for large spatial databases with noise, which applies to this study [55]. Then, each of the point cloud's clusters is further partitioned into voxels using the k-nearest

neighbor (KNN) algorithm. The voxelization step excludes the noise clusters determined by the DBSCAN algorithm. The clustering and voxelization processes are highly dependent on the minimum number of points per cluster/voxel and the neighborhood search radius, as shown in Figure 3.2. The neighborhood search radius for clustering is chosen based on the gaps between the objects and the structure-of-interest in the point cloud, so these objects and the structure-of-interest can be easily separated and assigned into mutually exclusive clusters. With respect to voxelization, the neighborhood search radius can be determined based on the spacing between the neighboring points in the vicinity of the structure-of-interest, minimum number of points per voxel, and the level of spatial resolution required in the full-field system identification (e.g., a neighborhood search radius of 1 cm will result into studying the dynamic response of the structure-of-interest at a centimeter level). Regarding the minimum number of points criterion, it aims to reduce the amount of noise in both the clustering and voxelization steps, as increasing the number of points per cluster/voxel will enhance the results. Overall, the clustering and voxelization hyperparameters can be set by the analyst based on the spatial density of the dynamic point cloud in the vicinity of the structure-of-interest and the level of spatial resolution required. In this study, the minimum number of points per cluster and voxel was assigned to 5 and 2, respectively, and the neighborhood search radii were 30 and 5 cm for clustering and voxelization, respectively. These parameters were determined based on the size of the structure and scanner-based parameters considered in the experimental program. The spatial clustering and voxelization steps are necessary to create a higher level of data representation for the 2D point clouds, which allows analysts to smoothly isolate the structure-of-interest from the background. Analysts can easily use voxels along the structure-of-interest to individually study the dynamic response of any part of the structure-of-interest for a careful assessment of the overall structural integrity at a high spatial resolution. The

proposed spatial clustering and voxelization algorithm is computationally efficient and easily scalable to monitor a wide range of civil infrastructure systems.

The cluster and voxel indices of each datapoint in the reference 2D point cloud are used to cluster and voxelize the entire dynamic point cloud efficiently, as shown in Figure 3.4. To extract the dynamic response of each voxel (i.e., change detection), the median of the points in a voxel at any time "t" is compared to the corresponding point in the reference frame (i.e., 2D point cloud at time $t = 0$) to quantify the dynamic motion, as detailed in Figure 3.3. Only the medians of the voxels were tracked in the change detection step, rather than all the voxel points, to make the dynamic motion extracted more robust to the scanner's noise. Voxels with dynamic displacements greater than 0.5 m were excluded from the analysis as these correspond to non-structural objects that abruptly moved during the dynamic monitoring. The change detection algorithm determines the dynamic motion of each voxel in both the Y and Z directions. The final output is a displacement time history of each voxel along the structure-of-interest.

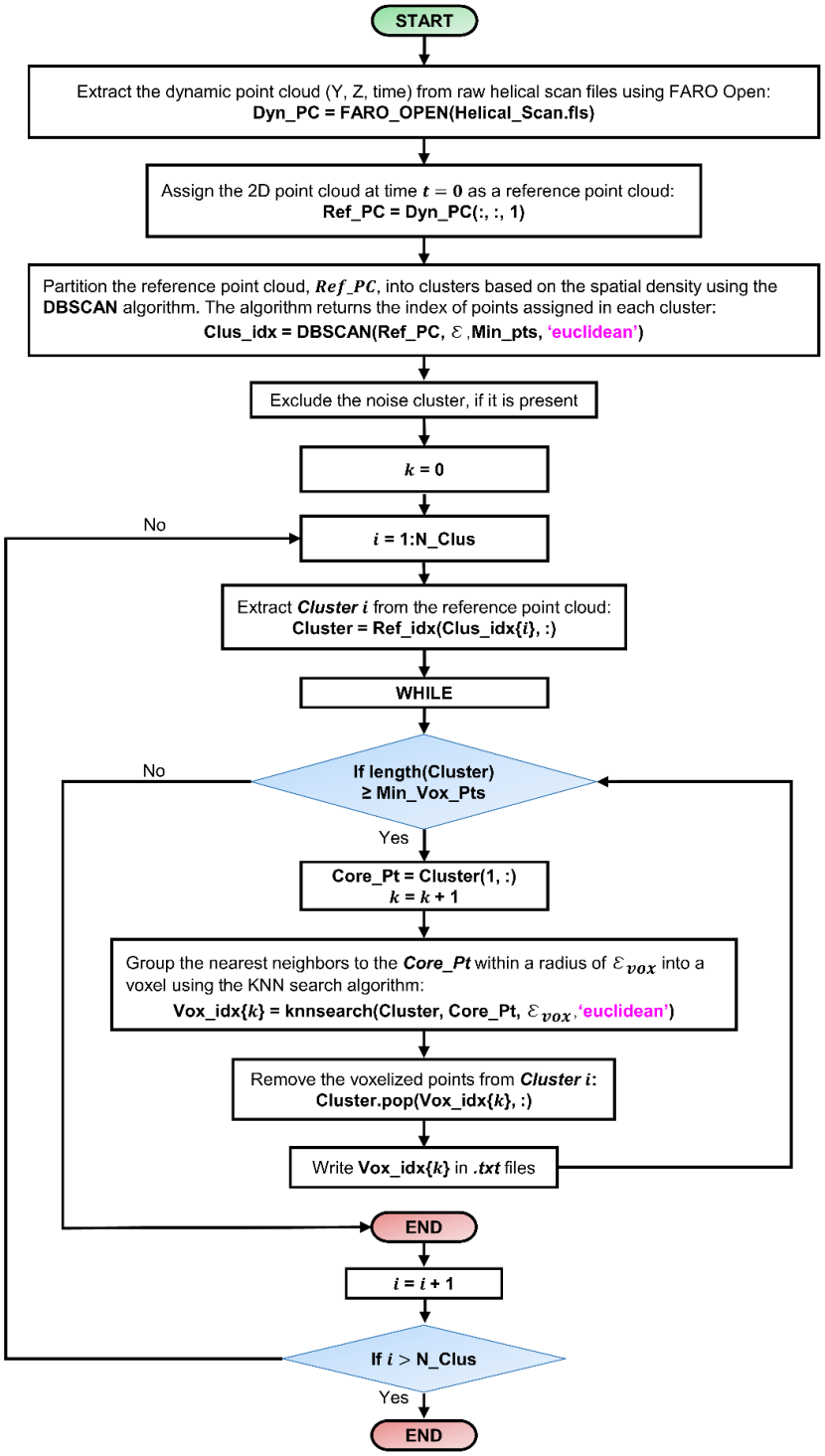

Figure 3.3 Spatial clustering and voxelization algorithm, where $Clus\_idx$: cluster indices of each data point in the reference point cloud (Ref_PC), ε: neighborhood search radius for clustering, Min_pts: minimum number of neighbors to identify a core point in each cluster, N_Clus: number of clusters in Ref_PC, Vox_Min_Pts: minimum number of points in each voxel, Vox_idx: voxel indices of each data point in each cluster, ε_{vox}: neighborhood search radius for voxelization, and $Core\_Pt$: core point in each voxel.

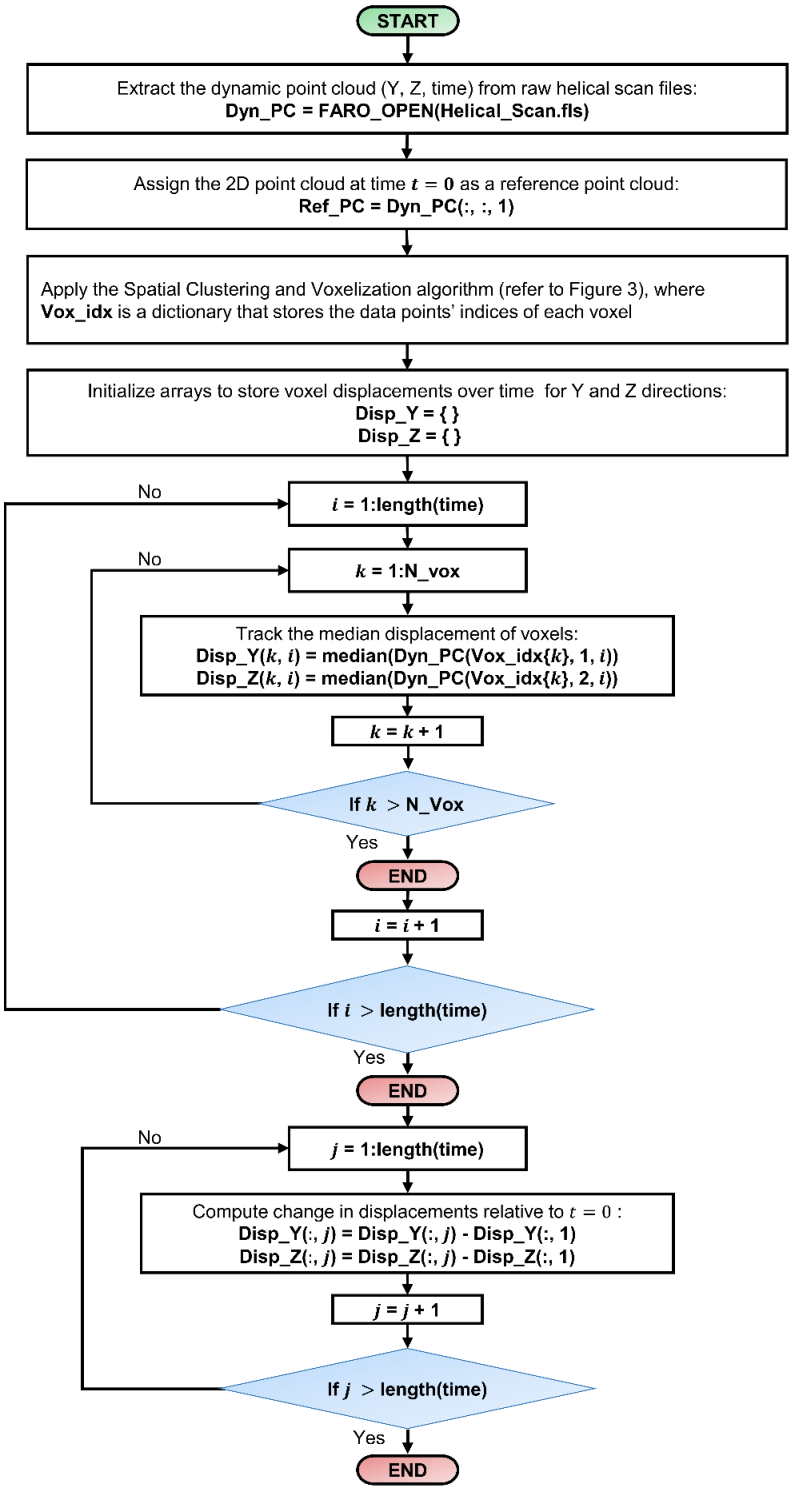

Figure 3.4 Change detection algorithm, where $Disp\_Y$: response history in the "Y" direction, $Disp\_Z$: response history in the "Z" direction, and N_vox: number of voxels in the reference point cloud (Ref_PC)

Chapter 4 Experimental Testing

This chapter discusses the experimental program conducted to validate the proposed framework for dynamic measurements monitoring using GBL. The experimental data were processed in both the time and frequency domains to understand the impact of scanner- and structure-based parameters on the accuracy of the results. Statistical analyses were conducted to interpret trends in data, if present.

4.1 Experimental Program

The main objective of this section is to investigate the effects of structure- and scanner-based parameters on the robustness of the proposed GBL-based dynamic monitoring framework through experimentation. A 2.45-m tall reconfigurable HSS 101.6×101.6×9.53 mm steel tower was used as the specimen in this study, where 304.8×76.2×50.8 mm steel rectangular weight plates were used to vary the dynamic properties of the steel tower during testing, as shown in Figure 4.1a. Figure 4.1b shows a sample of the tower's helical point cloud generated at a given instant in time. The lidar scanner parameters considered include the resolution, quality, and point-to-point distance of the 2D point clouds generated.

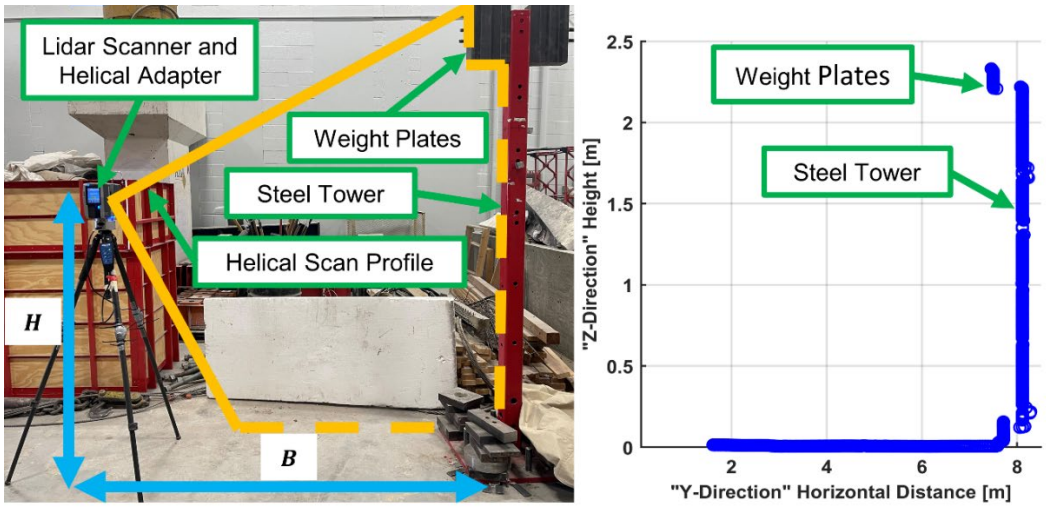

(a) (b)

Figure 4.1 (a) Helical scan setup, (b) helical point cloud

Table 4.1 shows the quality and resolution combinations considered in the experimentation task of this study. The quality parameter refers to the number of measurements the scanner makes to confirm point data [56], where high quality (i.e., 4) indicates more accurate range measurements. However, the scan time becomes significantly longer and consequently the sampling frequency is significantly reduced for higher quality and resolution scan settings, since the sampling frequency is inversely proportional to quality and resolution, as shown in Table 4.2. Generally, the point-to-point distance of a point cloud is defined as the distance between two neighboring points. Hence, varying the scan's point-to-point distance will affect the density and the number of points (i.e., spatial resolution) scanned along the structure-of-interest, which may impact the final modal analysis. The point-to-point distance of the point cloud in the vicinity of the structure-of-interest is explicitly controlled by the point cloud's resolution, the scanner's height above the ground "*H*", and the scanner's standoff horizontal distance from the structure "*B*". Hence, to extensively study the significance of the point-to-point distance parameter, four different combinations of *H* and *B*

along with six different scan resolutions were considered to populate the test matrix, as shown in Tables 4.1 and 4.2.

Table 4.1 Test matrix: scanner height and horizontal distance parameters

Scanner Height H **[m]**	**Horizontal Distance** B **[m]**
0.57	4
1.35	8

Table 4.2 Test matrix: scanner-based parameters

Quality	Dynamic Point Cloud Resolution		Scanner Sampling Frequency [Hz]
	Angular Increment/Point [°]	No. of Points	
1	0.0351	8544	95.31
	0.0176	17088	47.66
	0.0088	34176	23.83
2	0.0702	4272	93.75
	0.0351	8544	46.88
	0.0176	17088	23.44
3	0.1404	2136	95.31
	0.0878	3418	59.57
	0.0702	4272	47.66
	0.0351	8544	23.83
4	0.1404	2136	47.66
	0.0878	3418	29.79
	0.0702	4272	23.83

To closely study the influence of the structure's dynamic characteristics on the accuracy of the proposed framework, six single-degree-of-freedom (SDOF) configurations of the steel tower with unique natural frequencies were considered in the experimental program. The SDOFs' natural frequencies range from 3.6 Hz to 7.8 Hz, which were meant to replicate the natural frequencies of typical civil infrastructure systems (e.g., bridges, buildings, etc.). Table 4.3 shows the details of each SDOF configuration. For each SDOF configuration, the scanner was used to monitor the free vibration response of the specimen for approximately 400 seconds. During each test, the specimen was subjected to an impulse load from a mallet at the top level approximately every 60 seconds for excitation. It shall be noted that the amplitude of excitation was not controlled throughout the experimental campaign. To validate the results of the GBL-based dynamic monitoring framework,

PCB 352C34 accelerometers, and an Optotrak Certus motion capture system (i.e., infrared-based sensors) were used in the experiments. The PCB 352C34 model has a sensitivity of (±5%) 100 mV/g, measurement range of ±50g, and a frequency range of (±5%) 0.5 Hz – 10 kHz. The Optotrak system has a 3D accuracy of 0.1 mm, and was used in several previous studies to monitor the dynamic response of large-scale laboratory structures. The accelerometers and Optotrak markers were mounted on the specimen at three levels (i.e., 1.55, 1.82, and 2.45 m), and their sampling frequencies were 2048 and 128 Hz, respectively.

Table 4.3 Test matrix: SDOF configurations of the tower specimen

Configuration No.	**No. of Weight Plates**	**Natural Frequency estimated via Accelerometers [Hz]**
1	24	3.69
2	20	4.03
3	16	4.45
4	12	5.03
5	8	6.01
6	4	7.64

4.2 Results and Discussion

The main goal of this section is to validate the lidar results in light of the accelerometer and Optotrak results in both the time and frequency domains. For each test, the dynamic response of the voxels in the vicinity of the three height levels at which accelerometer and Optotrak sensors were placed, 1.55, 1.82, and 2.45m, were extracted using the novel two-step spatio-temporal algorithm developed. Figure 4.2 shows sample results of the spatial clustering and voxelization algorithms. The raw point cloud was clustered using a neighborhood search radius of 30 cm and a

minimum number of 5 points. These parameters were assigned based on the distance between the specimen and the neighboring objects in its vicinity, as 30 cm was sufficient to isolate the specimen's cluster from the background. Figure 4.2b shows the clustering results, where each color represents a mutually exclusive cluster. Regarding voxelization, the neighborhood search radius was assigned to 5 cm, so the minimum number of points per voxel (i.e., 2) can be maintained across all GBL parameters while providing high-spatial resolution results. Figure 4.2c shows an example of the specimen's voxelization results.

Although the comparative analysis showed very similar results and trends across all the height levels and sensing modalities, only the middle voxels, accelerometers, and Optotrak markers (i.e., at the height level of 1.82 m) are presented in the following sub-sections for consistency and conciseness. The middle voxel was selected, rather than the top voxel, due to consistent capture across tests. The voxels at the top level were in the vicinity of a sharp corner of the structure, which resulted in the top voxels to be missing in a handful of tests.

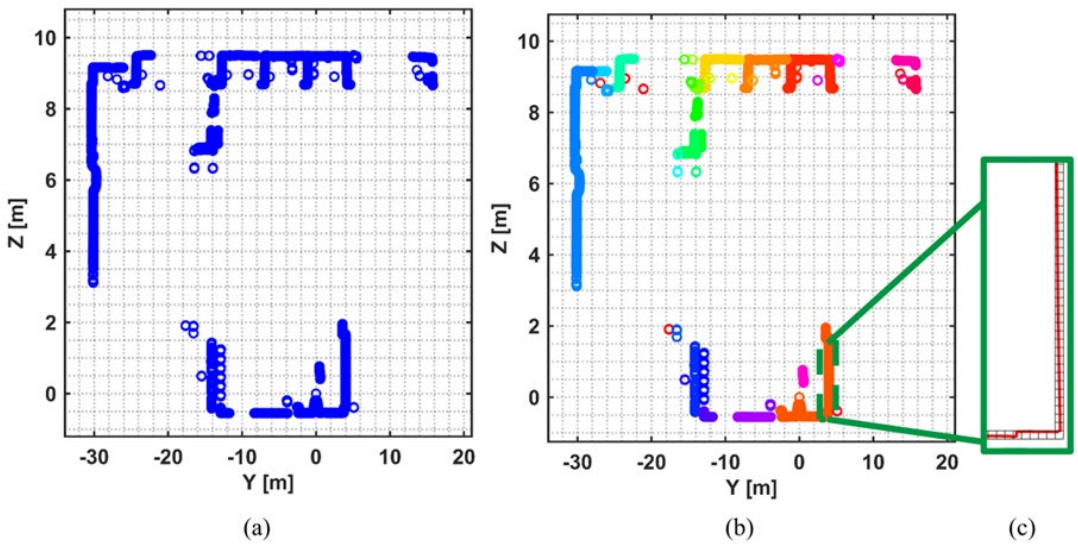

Figure 4.2 (a) Raw point cloud of the experimental setup, (b) spatially-clustered point cloud, (c) voxelized point cloud of the specimen

4.2.1 Dynamic Displacements

Figure 4.3 shows an example of the tower displacement detected by the lidar and Optotrak during a typical test. The plot indicates that both the lidar and Optotrak displacements were in strong agreement. Although the lidar displacements were noisier than those of the Optotrak, both the lidar and Optotrak measured similar amplitudes at the beginning of each excitation, which demonstrates the accuracy of lidar dynamic measurements at higher levels of excitation and the capability of detecting sub-millimeter displacements.

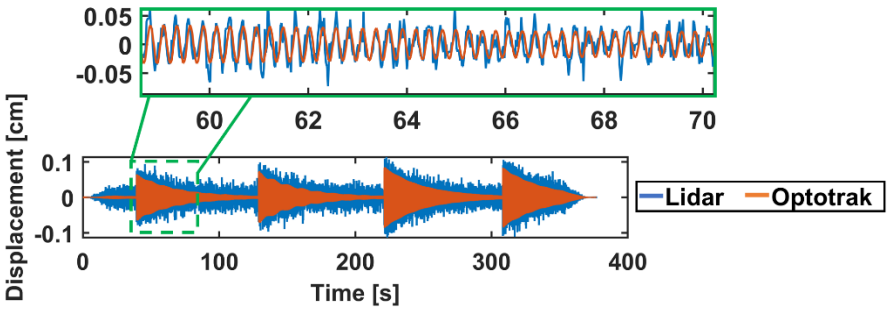

Figure 4.3 Sample time history of the vibration at the top of the steel tower under excitation

4.2.2 Operational Modal Analysis

4.2.2.1 Impact of Scanner-based Parameters

This section aims to statistically analyze the effect of the previously introduced scanner parameters: resolution, quality, and point-to-point distance on the accuracy of the proposed GBL-based dynamic monitoring framework. To quantify the impact of each of these parameters, the natural frequencies estimated via lidar (f_{Lidar}), accelerometers (f_{Accel}), and Optotrak (f_{Opt}) for each test were compared to one another. It shall be noted that the lidar measurements considered herein were not corrected with respect to those of the Optotrak (as discussed in the Displacement section), so the impact of lidar noise on the accuracy of the operational modal analysis results can

be studied independently of any signal denoising approaches. This is particularly useful to understand the potential impact of lidar noise in applications where reference displacement sensors might not be available (i.e., field monitoring of real-world structures). The natural frequencies were estimated by applying the classical peak-picking approach to the PSD plots of the processed data, where the PSD plots were generated using the Welch method (as explained in the Signal-to-Nose section). Figures 4.4a and b show that all tests yielded at most 0.4% difference in natural frequencies with the large majority of tests estimating natural frequencies by lidar within 0.02% of both accelerometer-based and Optotrak-based estimates. This indicates that GBL mostly estimates the natural frequencies of civil structures with a three-point decimal accuracy, which is widely acceptable in civil engineering applications. Moreover, by closely analyzing Figures 4.4a, b, and c together, it can be concluded that the relative difference between lidar- and accelerometer-based estimates was similar to those between the Optotrak and accelerometers. Therefore, these error levels are typical across different sensing modalities and are not unique to the GBL technique. The natural frequencies estimated via the accelerometers, Optotrak, and GBL for all the experiments are presented in the Appendix.

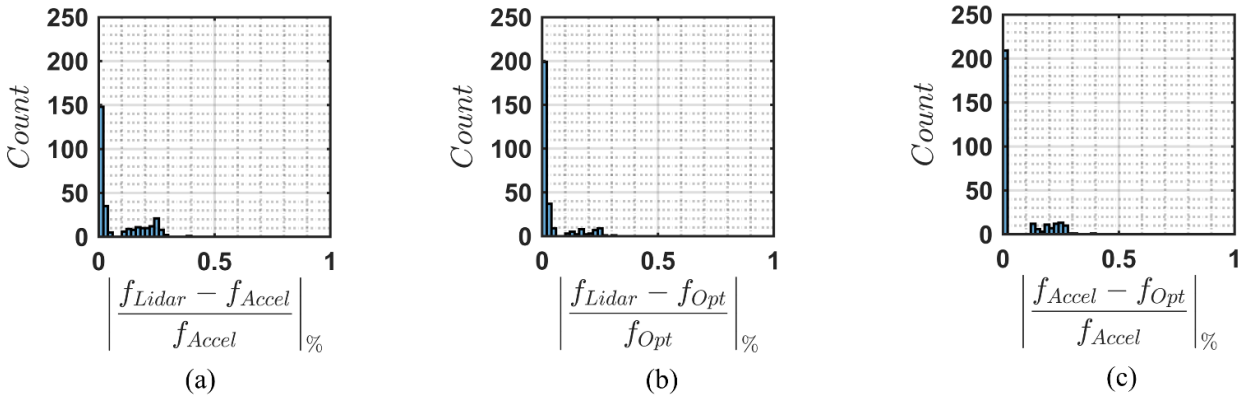

Figure 4.4 System identification results: (a) lidar versus accelerometers, (b) lidar versus Optotrak, and (c) Optotrak versus accelerometers

Figure 4.5 shows the relative difference between the lidar- and accelerometer-estimated natural frequencies for each test plotted as a function of the resolution, quality, and point-to-point distance of the point cloud for each respective test. It should be noted that the maximum point-to-point distance refers to the maximum distance between any two neighboring points along the height of the tower specimen, which changes based on the attributes of each respective test. Linear regression models and p-value analyses were used to understand the impact of each GBL parameter on the accuracy of the natural frequencies estimated via the GBL across all the experiments (see Tables 4.1, 4.2, and 4.3 for details on the test matrix considered herein). The results show nearly no correlation (i.e., R^2 and $\beta_1 = \sim 0$) between any of the scanner parameters and the relative difference between the lidar- and accelerometer-estimated natural frequencies. Furthermore, the p-value analyses show that the relationships between the accuracy of the GBL-based natural frequencies and the resolution, quality, and point-to-point distance of the point cloud are statistically not significant at a significance level of 1% ($p > 0.01$), as shown in Figure 4.5. These results suggest that the GBL-based parameters do not have an influence on the accuracy of the operational modal analysis, which indicates the robustness of the proposed GBL-based dynamic monitoring framework considering the conducted experiments. However, future field tests on structures of complex geometries and dynamical systems (i.e., bridges, buildings) with scans of larger maximum point-to-point distances are needed to rigorously examine the impact of the scanner parameters on the accuracy of the system identification results.

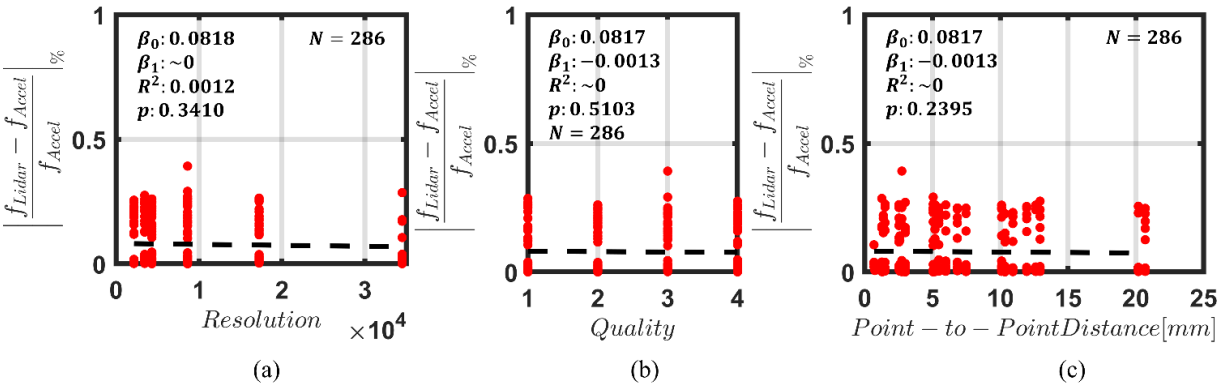

Figure 4.5 Summary results of scanner parameters: (a) resolution, (b) quality, and (c) maximum point-to-point distance along the tower specimen, where the dashed lines are trendlines estimated using linear regression

4.2.2.2 Impact of Structure Natural Frequency

The main objective of this section is to discuss the impact of the structure's natural frequency on the accuracy of the proposed GBL framework. Similar to the previous section, the relative difference between the lidar- and accelerometer-estimated natural frequencies will be considered the accuracy metric. Linear regression models and p-value analyses were used to statistically analyze the results. Figure 4.6 shows the distribution of the relative difference as a function of the structure's natural frequency estimated via the accelerometer (f_{Accel}) (i.e., ground truth), where the results show nearly no correlation (i.e., R^2 and $\beta_1 = \sim 0$). Furthermore, the p-value analyses show that the relationship between the accuracy of the GBL-based natural frequencies and the structure's natural frequency is statistically not significant at a significance level of 1% ($p > 0.01$), as shown in Figure 4.6. Hence, the results suggest that both the structure's natural frequency has nearly no impact on the results' accuracy for the tested specimen configurations (see Table 4.3).

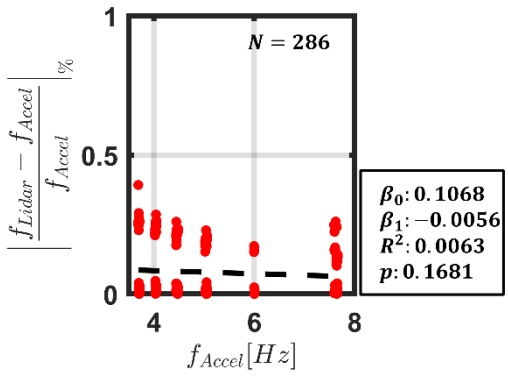

Figure 4.6 Summary results of the natural frequency estimation discrepancies as function of structure natural frequency results

Although the statistical analyses showed that the specimen's natural frequency had no impact on the accuracy of the GBL results, the tested specimen configurations were mainly simple SDOF-like structures, which did not include the excitation of modes beyond the fundamental mode of vibration. Therefore, structures of more complex dynamic systems need to be tested to gain more insights into the impact of the structure's dynamic characteristics on the results. This can be validated through field monitoring tests of real-world buildings and bridges, as such systems are difficult to replicate in the laboratory due to space limitations.

4.2.3 Operational Deflected Shapes

The frequency domain decomposition (FDD) method [57] was used to estimate the operational deflected shapes (ODS) of the tower specimen using the processed data of the accelerometers, Optotrak markers, and corresponding voxels at height levels: 1.55, 1.82, and 2.45 m (i.e., measurement degrees-of-freedom). The estimated ODS were compared to one another across all the sensing modalities using the modal assurance criterion (MAC) [58] as per Equation 2.

$$MAC(\{\varphi_r\},\{\varphi_s\}) = \frac{|\{\varphi_r\}^{\mathrm{T}}\{\varphi_s\}|^2}{(\{\varphi_r\}^{\mathrm{T}}\{\varphi_r\})(\{\varphi_s\}^{T}\{\varphi_s\})} \quad (2)$$

The MAC analysis aims to evaluate the similarity between the lidar-estimated ODS and their accelerometer and Optotrak counterparts, where MAC values closer to one indicate nearly identical ODS, and values closer to zero indicate totally dissimilar ODS. Figures 4.7a and b show the histogram plots of the MAC values computed between the accelerometer and lidar ODS and between the accelerometer- and Optotrak-based ODS, respectively. The plots show that the MAC values between the accelerometer- and lidar-based ODS were nearly identical to those between the accelerometers and Optotrak. Figure 4.7c shows samples of the estimated ODS, where the great agreement across all sensing modalities can be demonstrated.

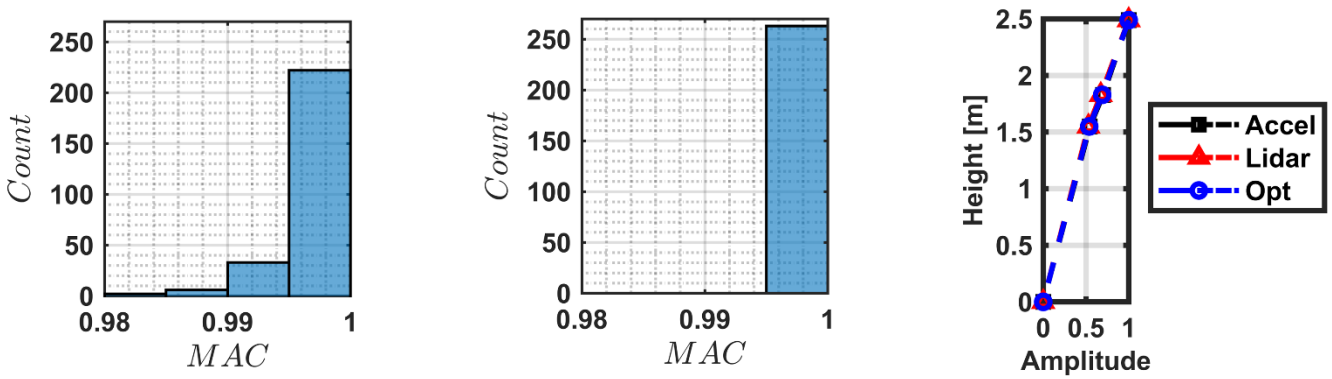

Figure 4.7 Summary results of Model Assurance Criterion: (a) lidar versus accelerometers, and (b) Optotrak versus accelerometers; (c) sample operational deflected shape

Chapter 5 Conclusions and Recommendations

5.1 Conclusions

Terrestrial Laser Scanners (GBL) can be employed to conduct full-field dynamic monitoring of civil structures for early damage detection and accurate finite element model updating applications. In this study, a novel end-to-end GBL-based dynamic monitoring framework was developed to monitor the dynamic response of civil structures remotely. The proposed framework was extensively investigated considering several scanner parameters (i.e., resolution, point-to-point distance, and quality) to monitor the free vibration response of six unique SDOF configurations in a controlled laboratory environment. In addition, an end-to-end novel two-step spatio-temporal algorithm was developed to autonomously extract the structural vibrations from the helical point clouds of the structures-of-interest, which enables the scalability of the proposed framework. The Optrotrak Certus motion capture system and high-sensitivity accelerometers were used to validate the GBL OMA results. Analytical and finite element models were used to validate the full-field dynamic response of the GBL. The comprehensive comparative analyses in both the time and frequency domains showed that the GBL results (i.e., displacements, natural frequencies, and operational deflected shapes) strongly agreed with those of the accelerometers and Optrotrak across all scanner-based parameters and SDOF configurations of the tower specimen despite the higher background noise levels of the GBL data. Furthermore, the full-field dynamic response of GBL was in great agreement with the high-fidelity mode shapes of the analytical and finite element models. The experimental results also highlight that the GBL was capable of detecting sub-millimeter structural vibrations, which indicates the potential of GBL to accurately monitor ambient vibrations of structures in the field. While the statistical analyses showed that GBL- and structure-based parameters had nearly no impact on the accuracy of the

GBL system identification results, it shall be noted that the specimen configurations considered in the experiments were SDOF-like structures with a relatively narrow range of natural frequencies (i.e., between 3.6 and ~8 Hz). The tested specimen configurations did not exhibit the excitation of modes beyond the fundamental mode of vibration. Also, the input excitations were impulsive and within the range of ±1 millimeter. While impulsive excitations can simulate the response of real-world bridges in the field due to traffic, this type of excitation does not replicate the typical ambient vibration response (i.e., non-impulsive response histories) of buildings due to wind or live load. Therefore, further research is warranted on full-scale structures in the field to evaluate the full extents of the GBL capabilities for dynamic monitoring of civil structures with respect to both structure and scanner-based parameters, and the amplitude and type of excitation.

5.2 Future Work

The experimental results highlighted that the GBL was capable of detecting sub-millimeter structural vibrations, which indicates the potential of GBL to accurately monitor ambient vibrations of structures in the field. However, further research is warranted on full-scale structures in the field to evaluate the full extent of GBL capabilities for dynamic monitoring of civil structures with-respect-to both structure and scanner-based parameters. Also, frameworks need to be developed and validated to monitor the dynamic response of structures using lidar/depth cameras that are mounted on moving platforms (i.e., UAVs), as these have not been studied previously.

References

1. The ASCE's 2021 Report Card for America's Infrastructure, American Society of Civil Engineers, http://infrastructurereportcard.org, last accessed 202/01/14.

2. Doebling SW, Farrar CR, Prime MB. A summary review of vibration-based damage identification methods. Shock and vibration digest. 1998 Mar 1;30(2):91-105.

3. Fan W, Qiao P. Vibration-based damage identification methods: a review and comparative study. Structural health monitoring. 2011 Jan;10(1):83-111.

4. Friswell M, Mottershead JE. Finite element model updating in structural dynamics. Springer Science & Business Media; 1995.

5. Toksoy T, Aktan AE. Bridge-condition assessment by modal flexibility. Experimental Mechanics. 1994 Sep;34:271-8.

6. Farrar CR, Jauregui DA. Comparative study of damage identification algorithms applied to a bridge: II. Numerical study. Smart materials and structures. 1998 Oct 1;7(5):720.

7. Maeck J, De Roeck G. Dynamic bending and torsion stiffness derivation from modal curvatures and torsion rates. Journal of Sound and Vibration. 1999 Aug 5;225(1):153-70.

8. Bernal D, Gunes B. Flexibility based approach for damage characterization: benchmark application. Journal of Engineering Mechanics. 2004 Jan;130(1):61-70.

9. Catbas FN, Gul M, Burkett JL. Conceptual damage-sensitive features for structural health monitoring: laboratory and field demonstrations. Mechanical systems and signal processing. 2008 Oct 1;22(7):1650-69.

10. Ewins DJ. Modal testing: theory, practice and application. John Wiley & Sons; 2009.

11. Boulkaibet I, Mthembu L, Marwala T, Friswell MI, Adhikari S. Finite element model updating using the shadow hybrid Monte Carlo technique. Mechanical Systems and Signal Processing. 2015 Feb 1;52:115-32.

12. Kim RE, Moreu F, Spencer Jr BF. Hybrid model for railroad bridge dynamics. Journal of Structural Engineering. 2016 Oct 1;142(10):04016066.

13. Brownjohn JM, Magalhaes F, Caetano E, Cunha A. Ambient vibration re-testing and operational modal analysis of the Humber Bridge. Engineering Structures. 2010 Aug 1;32(8):2003-18.

14. Spencer Jr BF, Hoskere V, Narazaki Y. Advances in computer vision-based civil infrastructure inspection and monitoring. Engineering. 2019 Apr 1;5(2):199-222.

15. Xu Y, Brownjohn J, Kong D. A non-contact vision-based system for multipoint displacement monitoring in a cable-stayed footbridge. Structural Control and Health Monitoring. 2018 May;25(5):e2155.

16. Xu Y, Brownjohn JM. Review of machine-vision based methodologies for displacement measurement in civil structures. Journal of Civil Structural Health Monitoring. 2018 Jan;8:91-110.

17. Hoskere V, Park JW, Yoon H, Spencer Jr BF. Vision-based modal survey of civil infrastructure using unmanned aerial vehicles. Journal of Structural Engineering. 2019 Jul 1;145(7):04019062.

18. Dong CZ, Celik O, Catbas FN, O'Brien EJ, Taylor S. Structural displacement monitoring using deep learning-based full field optical flow methods. Structure and Infrastructure Engineering. 2020 Jan 2;16(1):51-71.

19. Feng D, Feng MQ. Computer vision for SHM of civil infrastructure: From dynamic response measurement to damage detection–A review. Engineering Structures. 2018 Feb 1;156:105-17.

20. Dong CZ, Celik O, Catbas FN. Marker-free monitoring of the grandstand structures and modal identification using computer vision methods. Structural Health Monitoring. 2019 Nov;18(5-6):1491-509.

21. Yoon H, Elanwar H, Choi H, Golparvar-Fard M, Spencer Jr BF. Target-free approach for vision-based structural system identification using consumer-grade cameras. Structural Control and Health Monitoring. 2016 Dec;23(12):1405-16.

22. Ye XW, Yi TH, Dong CZ, Liu T. Vision-based structural displacement measurement: System performance evaluation and influence factor analysis. Measurement. 2016 Jun 1;88:372-84.

23. Lee J, Lee KC, Cho S, Sim SH. Computer vision-based structural displacement measurement robust to light-induced image degradation for in-service bridges. Sensors. 2017 Oct 11;17(10):2317.

24. Wang J, Li G. Study on Bridge Displacement Monitoring Algorithms Based on Multi-Targets Tracking. Future Internet. 2020 Jan 8;12(1):9.

25. Sony S, Laventure S, Sadhu A. A literature review of next-generation smart sensing technology in structural health monitoring. Structural Control and Health Monitoring. 2019 Mar;26(3):e2321.

26. Yang Y, Dorn C, Mancini T, Talken Z, Kenyon G, Farrar C, Mascareñas D. Blind identification of full-field vibration modes from video measurements with phase-based video motion magnification. Mechanical Systems and Signal Processing. 2017 Feb 15;85:567-90.

27. Yang Y, Dorn C, Mancini T, Talken Z, Nagarajaiah S, Kenyon G, Farrar C, Mascareñas D. Blind identification of full-field vibration modes of output-only structures from uniformly-sampled, possibly temporally-aliased (sub-Nyquist), video measurements. Journal of Sound and Vibration. 2017 Mar 3;390:232-56

28. Yang Y, Dorn C, Farrar C, Mascareñas D. Blind, simultaneous identification of full-field vibration modes and large rigid-body motion of output-only structures from digital video measurements. Engineering Structures. 2020 Mar 15;207:110183.

29. Chen JG, Wadhwa N, Cha YJ, Durand F, Freeman WT, Buyukozturk O. Modal identification of simple structures with high-speed video using motion magnification. Journal of Sound and Vibration. 2015 Jun 9;345:58-71.

30. Chen JG, Davis A, Wadhwa N, Durand F, Freeman WT, Büyüköztürk O. Video camera–based vibration measurement for civil infrastructure applications. Journal of Infrastructure Systems. 2017 Sep 1;23(3):B4016013.

31. Sarrafi A, Mao Z, Niezrecki C, Poozesh P. Vibration-based damage detection in wind turbine blades using Phase-based Motion Estimation and motion magnification. Journal of Sound and vibration. 2018 May 12;421:300-18.

32. Wadhwa N, Rubinstein M, Durand F, Freeman WT. Phase-based video motion processing. ACM Transactions on Graphics (TOG). 2013 Jul 21;32(4):1-0.

33. Gueguen P, Jolivet V, Michel C, Schveitzer AS. Comparison of velocimeter and coherent lidar measurements for building frequency assessment. Bulletin of Earthquake Engineering. 2010 Apr;8:327-38.

34. Jatmiko J, Psimoulis P. Deformation Monitoring of a Steel Structure Using 3D Terrestrial Laser Scanner (TLS). In Proceedings of the 24th International Workshop on Intelligent Computing in Engineering, Nottingham, UK 2017 Jul 12 (pp. 10-12).

35. Lee J, Kim RE. Noncontact dynamic displacements measurements for structural identification using a multi-channel Lidar. Structural Control and Health Monitoring. 2022 Nov;29(11):e3100.

36. Vezočnik R, Ambrožič T, Sterle O, Bilban G, Pfeifer N, Stopar B. Use of terrestrial laser scanning technology for long term high precision deformation monitoring. Sensors. 2009 Dec;9(12):9873-95.

37. Mukupa W, Roberts GW, Hancock CM, Al-Manasir K. A review of the use of terrestrial laser scanning application for change detection and deformation monitoring of structures. Survey review. 2017 Mar;49(353):99-116.

38. Lague D, Brodu N, Leroux J. Accurate 3D comparison of complex topography with terrestrial laser scanner: Application to the Rangitikei canyon (NZ). ISPRS journal of photogrammetry and remote sensing. 2013 Aug 1;82:10-26.

39. Schäfer T, Weber T, Kyrinovic P, Zámecniková M. Deformation measurement using terrestrial laser scanning at the hydropower station of Gabcikovo. In INGEO 2004 and FIG Regional Central and Eastern European Conference on Engineering Surveying, Bratislava, Slovakia 2004 Nov 11.

40. Sarti P, Vittuari L, Abbondanza C. Laser scanner and terrestrial surveying applied to gravitational deformation monitoring of large VLBI telescopes' primary reflector. Journal of Surveying Engineering. 2009 Nov;135(4):136-48.

41. Teza G, Galgaro A, Zaltron N, Genevois R. Terrestrial laser scanner to detect landslide displacement fields: a new approach. International Journal of Remote Sensing. 2007 Aug 20;28(16):3425-46.

42. Silva MF, Green A, Morales J, Meyerhofer P, Yang Y, Figueiredo E, Costa JC, Mascareñas D. 3D structural vibration identification from dynamic point clouds. Mechanical Systems and Signal Processing. 2022 Mar 1;166:108352.

43. Chesebrough B, Dasari S, Green A, Yang Y, Farrar CR, Mascareñas D. Light Field Imaging of Three-Dimensional Structural Dynamics. In Structural Health Monitoring, Photogrammetry & DIC, Volume 6: Proceedings of the 36th IMAC, A Conference and Exposition on Structural Dynamics 2018 2019 (pp. 101-108). Springer International Publishing.

44. Singh, Ashbindu. "Review article digital change detection techniques using remotely-sensed data." International journal of remote sensing 10, no. 6 (1989): 989-1003.

45. Xiao, Wen, Bruno Vallet, Mathieu Brédif, and Nicolas Paparoditis. "Street environment change detection from mobile laser scanning point clouds." ISPRS Journal of Photogrammetry and Remote Sensing 107 (2015): 38-49.

46. Lu, Dengsheng, Guiying Li, and Emilio Moran. "Current situation and needs of change detection techniques." International Journal of Image and Data Fusion 5, no. 1 (2014): 13-38

47. Mishra, Shivangi, Priyanka Shrivastava, and Priyanka Dhurvey. "Change detection techniques in remote sensing: A review." International Journal of Wireless and Mobile communication for Industrial systems4, no. 1 (2017): 1-8.

48. Coppin, Pol, Inge Jonckheere, Kristiaan Nackaerts, Bart Muys, and Eric Lambin. "Review ArticleDigital change detection methods in ecosystem monitoring: a review." International journal of remote sensing25, no. 9 (2004): 1565-1596.

49. Girardeau-Montaut, Daniel, Michel Roux, Raphaël Marc, and Guillaume Thibault. "Change detection on points cloud data acquired with a ground laser scanner." International Archives of Photogrammetry, Remote Sensing and Spatial Information Sciences 36, no. 3 (2005): W19.

50. Lague, Dimitri, Nicolas Brodu, and Jérôme Leroux. "Accurate 3D comparison of complex topography with terrestrial laser scanner: Application to the Rangitikei canyon (NZ)." ISPRS journal of photogrammetry and remote sensing 82 (2013): 10-26.

51. Du, Shouji, Yunsheng Zhang, Rongjun Qin, Zhihua Yang, Zhengrong Zou, Yuqi Tang, and Chong Fan. "Building change detection using old aerial images and new LiDAR data." Remote Sensing 8, no. 12 (2016): 1030.

52. Pirasteh, Saied, Pejman Rashidi, Heidar Rastiveis, Shengzhi Huang, Qing Zhu, Guoxiang Liu, Yun Li, Jonathan Li, and Erfan Seydipour. "Developing an algorithm for buildings extraction and determining changes from airborne LiDAR, and comparing with R-CNN method from drone images." Remote Sensing 11, no. 11 (2019): 1272.

53. Aijazi, Ahmad Kamal, Paul Checchin, and Laurent Trassoudaine. "Segmentation based classification of 3D urban point clouds: A super-voxel based approach with evaluation." Remote Sensing 5, no. 4 (2013): 1624-1650

54. Mukupa, Wallace, Gethin W. Roberts, Craig M. Hancock, and Khalil Al-Manasir. "A review of the use of terrestrial laser scanning application for change detection and deformation monitoring of structures." Survey review 49, no. 353 (2017): 99-116.

55. Ester M, Kriegel HP, Sander J, Xu X. A density-based algorithm for discovering clusters in large spatial databases with noise. In kdd 1996 Aug 2 (Vol. 96, No. 34, pp. 226-231).

56. Faro. Faro Laser Scanner Focus 3D X130 User Manual, available online: https://knowledge.faro.com, last accessed 2023/01/14.

57. Brincker R, Zhang L, Andersen P. Modal identification from ambient responses using frequency domain decomposition. InProceedings of the 18th international modal analysis conference (IMAC) 2000 Feb 7 (Vol. 1, pp. 625-630).

58. Allemang RJ. A correlation coefficient for modal vector analysis. InProc. of the 1st IMAC 1982 (pp. 110-116).

Appendix A Additional Experimental Results

Table A.1 Accelerometer results for test configuration $H = 0.57\text{m}$ and $B = 4\text{m}$

Quality	Resolution (No. of Points)	Natural Frequency [Hz]					
		Structural Configuration					
		1	**2**	**3**	**4**	**5**	**6**
1	8544	3.7013	4.0416	4.4624	5.0475	6.002	7.6075
	17088	3.6893	4.0514	4.4624	5.0495	6.0059	7.6138
	34176	3.6991	4.0514	4.4624	5.0495	5.9988	7.6064
2	4272	3.6991	4.0514	4.4624	5.0495	6.0017	7.6213
	8544	3.6991	4.0416	4.4624	5.0495	5.996	7.6035
	17088	3.6991	4.0416	4.4526	5.0495	5.9999	7.5948
3	2136	3.6979	4.0514	4.4624	5.0495	6.0001	7.5971
	3418	3.6991	4.0416	4.4624	5.0495	5.9969	7.5949
	4272	3.6991	4.0416	4.4624	5.0495	6.0008	7.5953
	8544	3.6991	4.0416	4.4624	5.0495	5.9969	7.6097
4	2136	3.6991	4.0514	4.4526	5.0495	6.0028	7.6006
	3418	3.6991	4.0416	4.4624	5.0495	6.0002	7.5879
	4272	3.6991	4.0416	4.4624	5.0495	5.9963	7.6043

Table A.2 Optotrak results for test configuration $H = 0.57\text{m}$ and $B = 4\text{m}$

Quality	Resolution (No. of Points)	Natural Frequency [Hz]					
		Structural Configuration					
		1	**2**	**3**	**4**	**5**	**6**
1	8544	3.6913	4.0416	4.4624	5.0474	6.002	7.6072
	17088	3.6991	4.0416	4.4624	5.0495	6.0059	7.6018
	34176	3.6991	4.0416	4.4624	5.0495	5.9988	7.6064
2	4272	3.6991	4.0514	4.4624	5.0495	6.0017	7.6023
	8544	3.6991	4.0416	4.4624	5.0495	6.0057	7.603
	17088	3.6991	4.0416	4.4624	5.0495	6	7.6065
3	2136	3.6978	4.0416	4.4624	5.0495	6.0002	7.5967
	3418	3.6991	4.0416	4.4624	5.0495	6.0065	7.6066
	4272	3.6991	4.0416	4.4624	5.0495	6.0008	7.5952
	8544	3.6991	4.0416	4.4624	5.0495	5.9968	7.5976
4	2136	3.6991	4.0416	4.4624	5.0495	6.0026	7.6007
	3418	3.6991	4.0416	4.4624	5.0495	5.9998	7.6054
	4272	3.6991	4.0416	4.4624	5.0495	6.0058	7.6041

Table A.3 GBL results for test configuration $H = 0.57\text{m}$ and $B = 4\text{m}$

Quality	Resolution (No. of Points)	Natural Frequency [Hz]					
		Structural Configuration					
		1	2	3	4	5	6
1	8544	3.6913	4.0415	4.4622	5.0475	6.0018	7.6071
	17088	3.6986	4.0407	4.4622	5.0487	6.0051	7.6015
	34176	3.6979	4.0501	4.4609	5.0493	5.9977	7.604
2	4272	3.6989	4.051	4.4621	5.0493	6.0014	7.6015
	8544	3.6982	4.0411	4.4614	5.0583	6.0051	7.5918
	17088	3.6977	4.041	4.4611	5.0491	5.9989	7.5942
3	2136	3.698	4.0413	4.4622	5.0492	6.0095	7.6141
	3418	3.6987	4.0508	4.4623	5.0495	5.9965	7.5828
	4272	3.6985	4.0407	4.4617	5.0492	6.0004	7.5955
	8544	3.698	4.0403	4.4617	5.049	5.9955	7.5969
4	2136	3.6984	4.0411	4.4618	5.0492	6.0025	7.5996
	3418	3.6981	4.0412	4.4613	5.0481	5.9992	7.6068
	4272	3.6976	4.0505	4.4608	5.0474	6.0059	7.6045

Table A.4 Accelerometer results for test configuration $H = 1.35\text{m}$ and $B = 4\text{m}$

Quality	Resolution (No. of Points)	Natural Frequency [Hz]				
		Structural Configuration				
		1	2	3	4	6
1	8544	3.6893	4.0318	4.4437	5.03	7.6427
	17088	3.6991	4.0318	4.4428	5.0195	7.6428
	34176	3.6991	4.0318	4.4526	5.03	7.633
2	4272	3.6991	4.0318	4.4428	5.03	7.6428
	8544	3.6991	4.0318	4.4428	5.03	7.6372
	17088	3.6991	4.022	4.4428	5.0202	7.633
3	2136	3.6991	4.0299	4.4428	5.0378	7.633
	3418	3.6991	4.0318	4.4428	5.0202	7.633
	4272	3.6926	4.022	4.4526	5.0202	7.633
	8544	3.6903	4.0318	4.4428	5.0202	7.6372
4	2136	3.6991	4.0318	4.4526	5.0202	7.633
	3418	3.6893	4.022	4.4428	5.0244	7.633
	4272	3.6991	4.0318	4.4428	5.03	7.633

Table A.5 Optotrak results for test configuration $H = 1.35\text{m}$ and $B = 4\text{m}$

Quality	Resolution (No. of Points)	Natural Frequency [Hz]				
		Structural Configuration				
		1	2	3	4	6
1	8544	3.6991	4.0318	4.4437	5.03	7.6428
	17088	3.6991	4.0318	4.4526	5.0289	7.6428
	34176	3.6991	4.0318	4.4526	5.03	7.6428
2	4272	3.6991	4.0318	4.4526	5.03	7.6428
	8544	3.6991	4.0318	4.4526	5.03	7.6371
	17088	3.6991	4.0318	4.4428	5.03	7.633
3	2136	3.6991	4.0297	4.4526	5.0263	7.633
	3418	3.6991	4.0318	4.4526	5.03	7.633
	4272	3.7021	4.0318	4.4526	5.03	7.633
	8544	3.7044	4.0318	4.4428	5.03	7.6371
4	2136	3.6991	4.0318	4.4428	5.03	7.6428
	3418	3.6991	4.0318	4.4428	5.0243	7.633
	4272	3.6991	4.0318	4.4428	5.03	7.633

Table A.6 GBL results for test configuration $H = 1.35\text{m}$ and $B = 4\text{m}$

Quality	Resolution (No. of Points)	Natural Frequency [Hz]				
		Structural Configuration				
		1	2	3	4	6
1	8544	3.6989	4.0217	4.4432	5.0298	7.6426
	17088	3.6982	4.0316	4.4521	5.0283	7.6419
	34176	3.698	4.0303	4.4509	5.029	7.6411
2	4272	3.6988	4.0315	4.4522	5.0199	7.6426
	8544	3.6986	4.0317	4.452	5.0295	7.6363
	17088	3.698	4.0309	4.4506	5.0278	7.6311
3	2136	3.6989	4.0298	4.4524	5.0262	7.6327
	3418	3.6985	4.022	4.4422	5.0297	7.623
	4272	3.7018	4.0313	4.4519	5.0296	7.6319
	8544	3.7047	4.03	4.4425	5.0294	7.6378
4	2136	3.6985	4.0315	4.4423	5.0296	7.6421
	3418	3.6985	4.0305	4.4411	5.0241	7.6306
	4272	3.7076	4.0299	4.4425	5.0295	7.6411

Table A.7 Accelerometer results for test configuration $H = 0.57\text{m}$ and $B = 8\text{m}$

Quality	Resolution (No. of Points)	Natural Frequency [Hz]					
		Structural Configuration					
		1	2	3	4	5	6
1	8544	3.7098	4.036	4.4824	5.0575	5.999	7.651
	17088	3.7136	4.0345	4.4699	5.0609	6.0041	7.6435
	34176	3.7126	4.0359	4.4748	5.0578	6.0012	7.6486
2	4272	3.7089	4.0393	4.478	5.0601	6.0058	7.6499
	8544	3.7169	4.0391	4.4779	5.0553	5.9981	7.6475
	17088	3.7154	4.0406	4.4771	5.0478	5.9994	7.6418
3	2136	3.7054	4.0452	4.4861	5.0574	6	7.6427
	3418	3.7115	4.041	4.4686	5.0582	6.0038	7.6402
	4272	3.7125	4.0413	4.4731	5.055	5.9943	7.649
	8544	3.7128	4.0432	4.481	5.0561	5.9996	7.6466
4	2136	3.7084	4.0384	4.4723	5.0613	6.0008	7.648
	3418	3.7029	4.0419	4.4746	5.0519	5.9951	7.6454
	4272	3.7086	4.0378	4.4669	5.0558	6.0009	7.6372

Table A.8 Optotrak results for test configuration $H = 0.57\text{m}$ and $B = 8\text{m}$

Quality	Resolution (No. of Points)	Natural Frequency [Hz]					
		Structural Configuration					
		1	2	3	4	5	6
1	8544	3.7096	4.036	4.4722	5.0573	5.9989	7.6506
	17088	3.7136	4.0344	4.4698	5.0607	6.0038	7.6534
	34176	3.7126	4.0358	4.4747	5.0575	6.0011	7.6484
2	4272	3.7089	4.0392	4.478	5.0601	6.0058	7.65
	8544	3.707	4.039	4.4778	5.0554	5.9981	7.6471
	17088	3.7155	4.0406	4.4771	5.0578	5.9992	7.6516
3	2136	3.7054	4.045	4.4758	5.0575	5.9998	7.6528
	3418	3.7113	4.041	4.4785	5.0582	6.0039	7.65
	4272	3.7125	4.0414	4.473	5.055	6.0042	7.6486
	8544	3.7126	4.0433	4.4709	5.0562	5.9997	7.6467
4	2136	3.7083	4.0382	4.4724	5.051	6.0009	7.6478
	3418	3.7131	4.0417	4.4746	5.0518	6.005	7.6453
	4272	3.7086	4.0376	4.4768	5.0557	6.0006	7.6472

Table A.9 GBL results for test configuration $H = 0.57\text{m}$ and $B = 8\text{m}$

Quality	Resolution (No. of Points)	Natural Frequency [Hz]					
		Structural Configuration					
		1	2	3	4	5	6
1	8544	3.7095	4.0465	4.4719	5.0576	6.0089	7.6609
	17088	3.7135	4.0347	4.4701	5.0601	6.0036	7.6529
	34176	3.7116	4.0362	4.4748	5.0568	6.0004	7.6491
2	4272	3.7086	4.0394	4.4778	5.0599	6.0057	7.6599
	8544	3.7073	4.0389	4.4774	5.0546	5.9982	7.6477
	17088	3.7146	4.0394	4.4773	5.0574	5.9999	7.6525
3	2136	3.7053	4.0352	4.4759	5.0571	6.0101	7.6522
	3418	3.7111	4.0312	4.4782	5.0584	6.0039	7.65
	4272	3.7119	4.0415	4.4728	5.0548	6.0033	7.6486
	8544	3.7116	4.0434	4.4799	5.0556	6.0096	7.6454
4	2136	3.7078	4.0382	4.472	5.0513	6	7.6478
	3418	3.7131	4.041	4.4742	5.0511	6.0054	7.6459
	4272	3.7086	4.0375	4.4771	5.0547	6.0009	7.6461

Table A.10 Accelerometer results for test configuration $H = 1.35\text{m}$ and $B = 8\text{m}$

Quality	Resolution (No. of Points)	Natural Frequency [Hz]				
		Structural Configuration				
		1	2	3	4	6
1	8544	3.7046	4.0334	4.4565	5.0506	7.6526
	17088	3.7073	4.0416	4.4624	5.0593	7.6624
	34176	3.7073	4.0416	4.4526	5.0495	7.6526
2	4272	3.7089	4.0335	4.4526	5.0537	7.6526
	8544	3.711	4.0416	4.4624	5.0457	7.6428
	17088	3.7044	4.0327	4.4572	5.0421	7.6526
3	2136	3.7126	4.0364	4.4624	5.0558	7.6526
	3418	3.7126	4.0435	4.4624	5.0495	7.6457
	4272	3.7096	4.0349	4.4624	5.0495	7.6624
	8544	3.6983	4.0304	4.4582	5.0448	7.6428
4	2136	3.705	4.0335	4.4616	5.0517	7.6526
	3418	3.7075	4.0443	4.445	5.0495	7.6526
	4272	3.7003	4.0459	4.4549	5.0495	7.6526

Table A.11 Optotrak results for test configuration $H = 1.35\text{m}$ and $B = 8\text{m}$

Quality	Resolution (No. of Points)	Natural Frequency [Hz]				
		Structural Configuration				
		1	2	3	4	6
1	8544	3.7143	4.0333	4.4566	5.0503	7.6526
	17088	3.7173	4.0318	4.4624	5.0495	7.6526
	34176	3.7072	4.0318	4.4624	5.0495	7.6526
2	4272	3.7089	4.0334	4.4624	5.0534	7.6526
	8544	3.711	4.0416	4.4624	5.0556	7.6526
	17088	3.7143	4.0327	4.4572	5.0518	7.6526
3	2136	3.7126	4.0363	4.4624	5.0456	7.6526
	3418	3.7124	4.0334	4.4624	5.0495	7.6554
	4272	3.7096	4.0348	4.4624	5.0495	7.6526
	8544	3.7092	4.0403	4.4583	5.0546	7.6526
4	2136	3.7049	4.0335	4.4615	5.0516	7.6526
	3418	3.7074	4.0442	4.4587	5.0495	7.6526
	4272	3.71	4.0459	4.4548	5.0495	7.6526

Table A.12 GBL results for test configuration $H = 1.35\text{m}$ and $B = 8\text{m}$

Quality	Resolution (No. of Points)	Natural Frequency [Hz]				
		Structural Configuration				
		1	2	3	4	6
1	8544	3.7143	4.0331	4.4567	5.0506	7.6618
	17088	3.7168	4.031	4.4617	5.0487	7.6522
	34176	3.7063	4.03	4.4605	5.0582	7.6497
2	4272	3.7185	4.0434	4.4621	5.0534	7.6524
	8544	3.7111	4.0315	4.4521	5.0457	7.6613
	17088	3.7137	4.0324	4.4561	5.0512	7.6615
3	2136	3.7123	4.0363	4.4622	5.0559	7.652
	3418	3.7127	4.0337	4.4622	5.0492	7.6451
	4272	3.7097	4.0347	4.4622	5.0492	7.6516
	8544	3.709	4.0301	4.4569	5.0546	7.6506
4	2136	3.7144	4.0428	4.461	5.0512	7.6512
	3418	3.7076	4.0436	4.4566	5.0489	7.652
	4272	3.7095	4.0463	4.4541	5.0474	7.6508